

The dynamic-thermal structures of the planetary boundary layer dominated by synoptic circulations and the regular effect on air pollution in Beijing

Yunyan Jiang^{*1,2}, Jinyuan Xin^{*1,2,3}, Ying Wang⁴, Guiqian Tang¹, Yuxin Zhao^{3,5}, Danjie Jia^{1,2}, Dandan Zhao^{1,2}, Meng Wang¹, Lindong Dai¹, Lili Wang¹, Tianxue Wen¹, Fangkun Wu¹

¹ State Key Laboratory of Atmospheric Boundary Layer Physics and Atmospheric Chemistry (LAPC), Institute of Atmospheric Physics, Chinese Academy of Sciences, Beijing 100029, China

² University of Chinese Academy of Sciences, Beijing 100049, China

³ Collaborative Innovation Center on Forecast and Evaluation of Meteorological Disasters, Nanjing University of Information Science & Technology, Nanjing, 210044, China

⁴ College of Atmospheric Sciences, Lanzhou University, Lanzhou 730000, China

⁵ Institute of Atmospheric Composition, Chinese Academy of Meteorological Science, Beijing 100081, China

* These authors contributed equally to this work.

* Correspondence: Jinyuan Xin; email: xjy@mail.iap.ac.cn; phone: (+86)010-62059568; address: #40 Huayanli, Chaoyang District, Beijing 100029, China

Abstract. To investigate the impacts of multiscale circulations on the planetary boundary layer (PBL), we have carried out the PBL dynamic-thermal structure field experiment with a Doppler Wind Profile Lidar, a microwave radiometer and a ceilometer from January 2018 to December 2019 in Beijing. We found that the direct regulatory effect of synoptic circulation worked through transporting and accumulating pollutants in front of mountains in the daytime. While the indirect effect of multiscale circulations worked through coupling mechanisms in the nighttime. The horizontal coupling of different direction winds produced a severe pollution convergent zone. The vertical coupling of upper environmental winds and lower regional breezes regulated the mixing and diffusion of pollutants by generating dynamic wind shear and advective temperature inversion. We also found that the dominated synoptic circulations led to great differences in PBL dynamic-thermal structure and pollution. The cyclonic circulation resulted in a typical multilayer PBL characterized by high vertical shear (600 m), temperature inversion (900 m) and an inhomogeneous stratification. Meanwhile, strong regional breezes pushed the pollution convergent zone to the south of Beijing. The southwesterly circulation resulted in a mono-layer PBL characterized by low vertical shear (400 m) and inversion (200 m). The westerly circulation led to a hybrid-structure PBL, and the advective inversion generated by the vertical shear of zonal winds. Strong environmental winds of southwesterly and westerly circulations pushed the severe pollution zone to the front of mountains. There was no distinct PBL structure under the anticyclone circulation. The study systematically revealed the appreciable effects of synoptic and regional circulations on PBL structure and air quality, which enriched the prediction theory of atmospheric pollution in the complex terrain.

Keywords Synoptic Circulation Types, Planetary Boundary Layer, Multiscale Circulations Coupling, Regional Breezes, Air Pollution

1. Introduction

Beijing megacity is the political, economic and cultural center of China. With the recent economic development and acceleration of urbanization, an increasing number of air pollution episodes have emerged and pose a direct threat to human health (Quan et al., 2014; Fu et al., 2014; Cheng et al., 2016; Song et al., 2017).

41 Large-scale atmospheric circulations play a leading role in the transportation, accumulation and dispersion of
42 pollution and thus result in the day-to-day variation of air quality (Tai et al., 2010; Zhang, 2017; Wang et al., 2018).
43 Zheng et al. (2015) explored the relationships between AOD and synoptic circulations and found that a uniform
44 surface pressure field in eastern China or a steady straight westerly in the middle troposphere is typically
45 responsible for heavy pollution events. Miao et al. (2017) specially targeted summertime synoptic types,
46 indicating that the horizontal transport of pollutants induced by the synoptic forcing is the most important factor
47 affecting the air quality of Beijing in summer. They also found that synoptic patterns with high-pressure systems
48 located to the east or southeast of Beijing are the most favorable types for heavy aerosol pollution events. Leung
49 et al. (2018) indicated that daily PM_{2.5} had strong positive correlation with temperature and relative humidity
50 but negative correlation with sea-level pressure in northern China. The PM_{2.5}-to-climate sensitivities results were
51 applied to predict future PM_{2.5} due to climate change, and found a decrease of 0.5 μg/m³ in annual mean PM_{2.5}
52 in the Beijing-Tianjin-Hebei region due to more frequent cold frontal ventilation. Liu et al. (2019) found that the
53 episodes of PM_{2.5} pollution over the Beijing-Tianjin-Hebei region in winter were related to weather patterns such
54 as the rear of a high-pressure system approaching the sea, a high-pressure field, a saddle pressure field, and the
55 leading edge of a cold front. Li et al. (2020) quantitatively analyzed the contributions of different large-scale
56 circulations to PM_{2.5}. Many approaches have been used to classify the synoptic circulations, which can be mainly
57 divided into subjective and objective methods. Objective weather typing methods have the advantages of
58 convenient operation, high objectivity and efficiency, hence they have been employed widely in recent years
59 (Zhang et al., 2016; Ye et al., 2016; Miao et al., 2017). In this study, we adopt an objective Lamb-Jenkinson
60 classification scheme to categorize the large-scale atmospheric circulations centered on Beijing. The
61 Lamb-Jenkinson approach, which is confirmed that the categorization results have clear physical understanding,
62 has been applied widely in previous studies (Huang et al., 2016; Liao et al., 2017; Yu et al., 2017).

63 In addition, Beijing is located in the North China Plain (NCP) region and surrounded by Yan and Taihang
64 Mountains to the north and west, respectively (Fig. 1b). The Bohai Sea lies to the southeast and is approximately
65 150 km from Beijing. This semibasin topography blocks and decelerates the relatively weak southerly airflows (Li
66 et al., 2007). Aerosol pollutants from southern provinces through regional transportation stagnate and converge
67 in front of the mountains, leading to the accumulation zone of pollution. This unique geographic location and
68 topography results in diurnal variations in the mountain-plain breeze (MPB) and sea-land breeze (SLB) under
69 relative weak synoptic circulations. The SLB can penetrate deep into the mainland when it is blooming, and
70 aerosol pollution transported previously over the sea could be recirculated to the Beijing-Tianjin-Hebei region (Liu
71 et al., 2009; Miao et al., 2017; Bei et al., 2018). As Beijing is surrounded by mountains and relatively far from the
72 Bohai Sea, the intensity of the MPB circulation is much stronger compared to the sea-land breeze circulation in
73 Beijing (Chen et al., 2009; Miao et al., 2015a, b), especially when synoptic circulations dominate in Bohai areas.
74 Miao et al. (2015b) found that the regional-scale MPB circulations can modulate aerosol pollution by lifting or
75 suppressing PBL. Chen et al. (2009) found that the MPB played an important role in the vertical transportation
76 and dispersion of pollutants via the mountain chimney effect.

77 The PBL structure is also a key factor affecting the distribution and intensity of pollutants in addition to the
78 circulations. The thermal structure of the PBL determines the vertical dispersion of aerosols. In the daytime
79 convective layer, air pollution tends to be mixed vertically and homogeneously because of intensified turbulence
80 and eddies of different sizes by radiation (Stull, 1988). After sunset, the turbulence decays and a stable boundary
81 layer forms with weak turbulence. A radiation inversion on the ground caps the pollutants and leads to the
82 accumulation near the surface. Hu et al. (2014) found that westerly warm advection above the Loess Plateau was
83 transported over the NCP and imposed a thermal inversion, which acted as a lid and capped the pollution in the
84 boundary layer (Xu et al., 2019). The dynamic structure of the PBL, including wind shears and turbulence, can

85 modify air quality by influencing the dispersion and transport processes of air pollutants (Li et al., 2019). Zhang et
86 al. (2020) found that a much weaker vertical wind shear was observed in the lower part of the PBL under polluted
87 conditions, compared with that under clean conditions, which could be caused by the strong ground-level PM_{2.5}
88 accumulation induced by weak vertical mixing in the PBL. In turn, the particulate matter can also affect the PBL
89 structure by scattering and absorbing of solar radiation, and lead to severe pollution by positive feedback (Petaja
90 et al, 2016; Li et al, 2017). Ding et al. (2016) suggested that black carbon enhanced haze pollution in megacities in
91 China by heating upper PBL and cooling surface. Lou et al. (2019) investigated the relationships between PBL
92 height and PM_{2.5} and indicated that the strongest anticorrelation occurred in the NCP region at 1400 Beijing
93 time.

94 To sum up, because of the unique topography and geographic location of Beijing, large-scale circulation
95 and regional-scale thermodynamic circulation both have appreciable impacts on PBL and air pollution. What are
96 the characteristics of PBL structure and the temporal and spatial distribution of pollution under different
97 circulation types, and how do the multiscale circulations jointly force the PBL structure to change when they
98 coexist are still unrevealed. Therefore, one objective of this study is to investigate the PBL dynamic-thermal
99 structure and the distribution of severe pollution area under the most frequent circulation types in Beijing. The
100 other primary objective is to further explore the synergetic effects of multiscale circulations on PBL and pollution
101 in detail. Since the weather typing approach is able to classify the synoptic circulations into different types and
102 the high vertical resolution remote sensing observations can measure the fine dynamic-thermal structures of PBL,
103 the objectives can be achieved by employing weather typing approach and remote sensing measurements as a
104 necessary first step. The remainder of this paper is organized as follows. Sect. 2 describes the instruments, data
105 and method. Sect. 3 classifies the synoptic circulation types and selects typical types as research objects.
106 Moreover, it further investigates how the coupling mechanism of synoptic circulations and regional-scale
107 circulations changes the dynamic and thermal PBL structure and air pollution. Sect. 4 discusses the improvements
108 on previous studies and summarizes the main findings.

109 2. Data and Method

110 A PBL field observation experiment was performed from January 2018 to December 2019 basing on
111 multiple remote sensing devices, including Doppler Wind Profile Lidar, microwave radiometer (MWR) and
112 ceilometer in the courtyard of the Institute of Atmospheric Physics (39.6°N and 116.2°E), Chinese Academy of
113 Sciences, Beijing (Fig. 1b). We systematically probed the PBL dynamic structure, thermodynamic structure and the
114 vertical distribution of aerosols using the Lidar three-dimensional winds, the MWR temperature and humidity
115 profiles and the ceilometer backscattering coefficient respectively. The original remote sensing data, with high
116 temporal and spatial resolution, are fully capable to show the fine PBL dynamic-thermal structure. The reanalysis
117 data of mean sea level pressure (MSLP) and winds are used to depict the synoptic circulations, and winds from
118 hundreds of automatic weather stations to characterize the fine regional circulations. Thus, the synergistic
119 impacts of coexisting synoptic-scale and regional-scale circulations on the PBL dynamic-thermal structure and air
120 pollution in Beijing megacity can be well understood using the remote sensing and meteorological data in
121 combination with the Lamb-Jenkinson weather typing approach. The typical cases lasting two days in the same
122 weather type (C, SW, W and A) are on October 22 to 24, July 26 to 28, May 15 to 17 in 2019 and December 28 to
123 30 in 2018 respectively. Due to the algorithm limitations on the observation conditions, the data of backscattering
124 coefficient and temperature profiles are missing about 5 hours on July 27, 2019.

125 2.1 Remote sensing data

126 The ceilometer (CL31, Vaisala) BL-VIEW software derives the PBL height according to the minimum value of
127 the local backscatter gradient (Tang et al., 2015), basing on the assumption that the aerosol concentration in

128 mixing layer (ML) is close to constant and significantly larger than that in the air above (Steyn et al., 1999). The
129 BL-VIEW algorithm excluded profiles with fog, precipitation or low clouds, therefore resulting in the missing value
130 of attenuated backscatter coefficient on July 27, 2019 used in southwesterly circulation. The vertical resolution of
131 the backscatter is 10 meters and the maximal detection range can reach 7.7 km. A full overlap is achieved by
132 using the same telescope for transmitting and receiving so that the backscatter can be used from the first range
133 gate (Münel et al, 2007). This gives a clear advantage over other commonly used Automatic Lidars and
134 Ceilometers that usually show great uncertainty in the range below 200–500 m (Kotthaus et al., 2018). Three
135 possible PBL heights, with a temporal resolution of 10 minutes, can be output simultaneously to characterize the
136 multiple aerosol layers structure according to the first three largest negative gradients of backscatter. The typical
137 uncertainty of CL31 on attenuated backscatter coefficient is $\pm 20\%$ and is ± 200 m on PBL height determination
138 compared with radiosonde and other active remote sensors (Tsaknakis et al., 2011).

139 A Windcube 100S scanning Doppler Lidar is used to measure the wind profiles basing on the Doppler shift
140 of aerosol particulate backscatter signals. Dai et al. (2020) suggested that the Doppler Wind Profile Lidar is fully
141 capable to measure three-dimensional winds by comparing with cup anemometer and sonic wind anemometer.
142 The vertical measuring range is from 50 m to 3.3 km. Several scanning modes are available and the DBS (Doppler
143 Beam Swinging technique) mode, which includes four LOS (lines of sight) spaced 90° apart with a fixed elevation
144 angle and one vertical LOS, is selected to detect the profiles of winds. The vertical resolution of the profiles is 25
145 m and the temporal resolution is 20 s. The velocity uncertainty along each LOS is associated with carrier-to-noise
146 ratio (CNR) for each measurement volume following the methodology from O'Connor et al. (2010). Typically, a
147 threshold of -22 or -23 dB is used as a limit for the accepted uncertainty in the Lidar measurements (Gryning et
148 al., 2016), which corresponds to an uncertainty of about 0.15 m s^{-1} (Aitken et al., 2012; Suomi et al., 2017).

149 The temperature and relative humidity profiles in RPG-HATPRO MWR are determined by neural network
150 (NN) algorithm, and the vertical resolution of the profiles is 10–30 m in the lowest 0.5 km, 40–90 m from 0.5 km
151 to 2.5 km, 100–200 m from 2 km to 10 km, and the temporal resolution is 1 s. The MWR used in this study has
152 been tested by comparing with radiosonde observations (Zhao et al., 2019). The systematic errors increase with
153 altitude, and the MWR-retrieved temperature and relative humidity are of quite high reliability inside the PBL.
154 The temperature biases and RMSEs are -2 – 0 °C and 1 – 2 °C under 2 km, and the minimum of biases and RMSEs are
155 between 1 km and 2 km, less than 0.5 °C and 1.3 °C respectively. Since the relative humidity derived from the
156 temperature and water vapor density, both the errors can cause the uncertainties. The bias and RMSE of relative
157 humidity is about -5% and 15% under 2 km. Furthermore, the residual liquid droplets on the water film led to
158 high brightness temperature measured by the MWR, resulting in the abnormal high values of the temperature
159 and humidity data. Therefore, data on July 27, 2019 were eliminated and substituted with missing values.

160 2.2 Meteorological data

161 The daily MSLP and wind at 850 hPa from the National Center for Atmospheric Research (NCAR) reanalysis
162 data (gridded at $2.5^\circ \times 2.5^\circ$) were used to classify the synoptic circulation patterns and depict the background
163 circulations of the typical circulation types. The divergence and vertical velocity reanalysis data (gridded at $1^\circ \times 1^\circ$)
164 with a temporal resolution of 1 h from Re-analysis Interim (ERA-Interim) of European Centre for Medium-Range
165 Weather Forecasts (ECMWF) were used to study the vertical motion in the mid-low troposphere in the NCP region
166 and its impact on PBL structure.. The hourly mean wind at the surface in the Beijing-Tianjin-Hebei area were
167 collected by hundreds of automatic weather stations operated by the China Meteorological Administration
168 (CMA).

169 2.3 Pollutant data

170 The hourly PM_{2.5} concentrations in the Beijing-Tianjin-Hebei monitoring sites are acquired from the
171 National Urban Air Quality Real-time Publishing Platform (<http://106.37.208.233:20035/>) issued by the Ministry of

172 Ecology and Environment. There are 35 air quality monitoring stations in Beijing (Fig. 4a) and 68 monitoring sites
 173 in Tianjin and Hebei provinces (Fig. 5, 7, 9). The PM_{2.5} concentration in Beijing are shown in shaded by
 174 interpolating data of 35 sites, while the PM_{2.5} concentration in other areas are shown in scatter with color as the
 175 spatial resolution is relative low. The PM_{2.5} data of Olympic Center station, which is the closest monitoring site to
 176 the location of remote sensing measurements (less than 1 km), is used in the circulation classification.

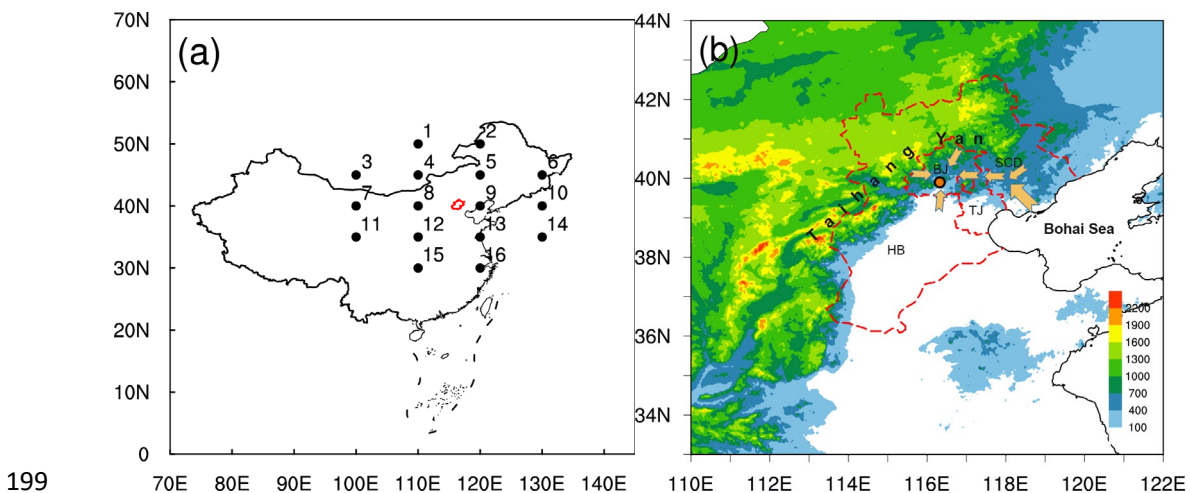
177 2.4 Method

178 The Lamb-Jenkinson weather typing (LWT) approach is widely adopted in large-scale circulation
 179 classification (Lamb 1972; Jenkinson and Collison, 1977) because of its automation and explicit meteorologically
 180 meaning. To classify the synoptic circulation types, the daily MSLP in 2018 and 2019 were used. The LWT scheme
 181 is a half-objective categorization method. The weather patterns are predefined and each day can be identified
 182 objectively as one certain type according to a small number of empirical rules (Trigo and DaCamara, 2000). As
 183 shown in Fig. 1a, 16 gridded pressure data surrounding the study area (Beijing city) were selected to calculate the
 184 direction and vorticity of geostrophic wind. The synoptic circulation can be classified into 26 types in total
 185 including two vorticity types (cyclonic, C; anticyclonic, A), eight directional types (northeasterly, NE; easterly, E;
 186 southeasterly, SE; southerly, S; southwesterly, SW; westerly, W; northwesterly, NW; and northerly, N), and sixteen
 187 hybrid types (CN, CNE, CE, CSE, CS, CSW, CW, CNW, AN, ANE, AE, ASE, AS, ASW, AW, and ANW).

188 The gradient Richardson number (Ri) is the ratio of the buoyancy term to the shear term in the turbulent
 189 kinetic equation. A negative Ri is an indication of buoyancy-generated turbulence, while positive Ri less than 0.25
 190 indicates shear turbulence and dynamic instability. When Ri is larger than 0.25 and less than 1.0 the flows
 191 become neutral, or exhibit hysteresis and still maintain turbulent. Otherwise, Ri larger than 1.0 means turbulent
 192 flow will turn to be dynamically stable laminar (Stull, 1988). The distributional characteristics of Ri can reveal
 193 whether the PBL has a stratified structure or not (Banakh et al., 2020). Thus, we adopt the critical values of 0.25
 194 and 1.0 as a criterion to determine the PBL structure. Ri can be calculated by Equation 1, where g is the
 195 acceleration of gravity and Δz is the height interval between adjacent layers. $\bar{\theta}$ is the mean virtual potential
 196 temperature, $\Delta \bar{u}$ and $\Delta \bar{v}$ is the mean zonal and meridional wind speeds within the height interval
 197 respectively.

198

$$Ri = \frac{\frac{g}{\bar{\theta}} \frac{\Delta \bar{\theta}}{\Delta z}}{\left(\frac{\Delta \bar{u}}{\Delta z}\right)^2 + \left(\frac{\Delta \bar{v}}{\Delta z}\right)^2} \quad (1)$$



200 Fig. 1 The locations of 16 grid data of the 5°× 10° MSLP used for Lamb-Jenkinson weather type classification (black
201 dots) (a). The terrain height of the North China Plain (shaded, units: m) (b). The location of Beijing city and the
202 Beijing-Tianjin-Hebei region is marked by the red solid lines and red dashed lines respectively. The orange dot
203 indicates the location of remote sensing devices. The arrows indicate the horizontal coupling mechanism of how
204 multiscale circulations affect pollution by generating convergent zone.

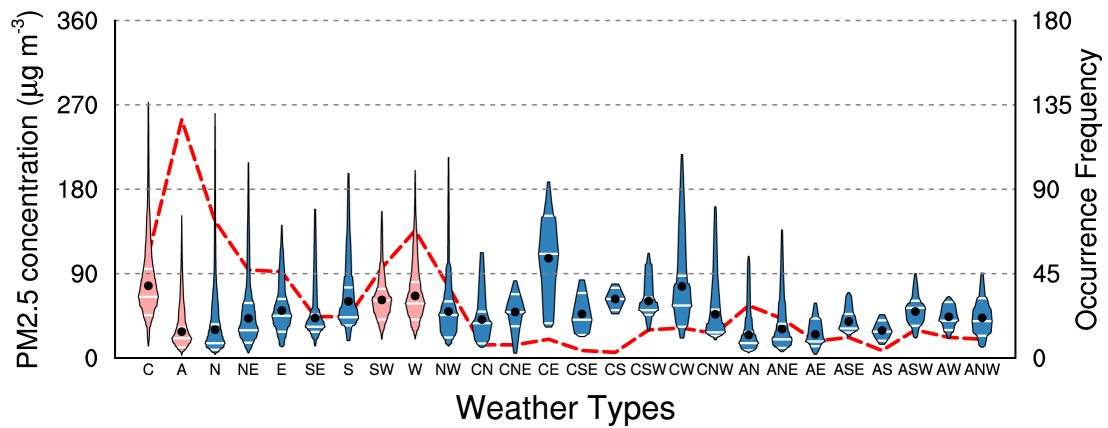
205 3. Results and Discussions

206 3.1 The typical weather types and PM2.5 distribution

207 Based on the Lamb-Jenkinson weather typing approach, synoptic circulations from 2018 to 2019 were
208 classified into predefined 26 circulation patterns and each day has a specific type. The distributional
209 characteristics of daily averaged PM2.5 concentration, as well as the occurrence frequency of different circulation
210 patterns, were statistically conducted. The occurrence frequencies of the two vorticity and eight directional types
211 were much higher than those of the other sixteen hybrid types, accounting for 75% of total days (Fig. 2).
212 According to the pollution intensity, three pollution types (cyclonic C, southwesterly SW and westerly W) and one
213 clean type (anticyclonic A) occurring most frequently in the NCP were selected as the studied circulation patterns.
214 It was consistent with the results of Li et al. (2020) on the relationship between pollutant concentration and
215 circulation types in northern China. Weather types with high PM2.5 concentration but occurring no more than
216 ten times, such as type CE and type CW, were not discussed in this article. The average and extreme PM2.5
217 concentrations of type C reached 77 $\mu\text{g}/\text{m}^3$ and 270 $\mu\text{g}/\text{m}^3$, respectively, and were much stronger than the other
218 pollution types. Clearly, the cyclonic circulation pattern was more conducive to severe pollution events. The
219 circulation of type A was the most common type, and the PM2.5 concentration was 28 $\mu\text{g}/\text{m}^3$, which was the
220 lowest.

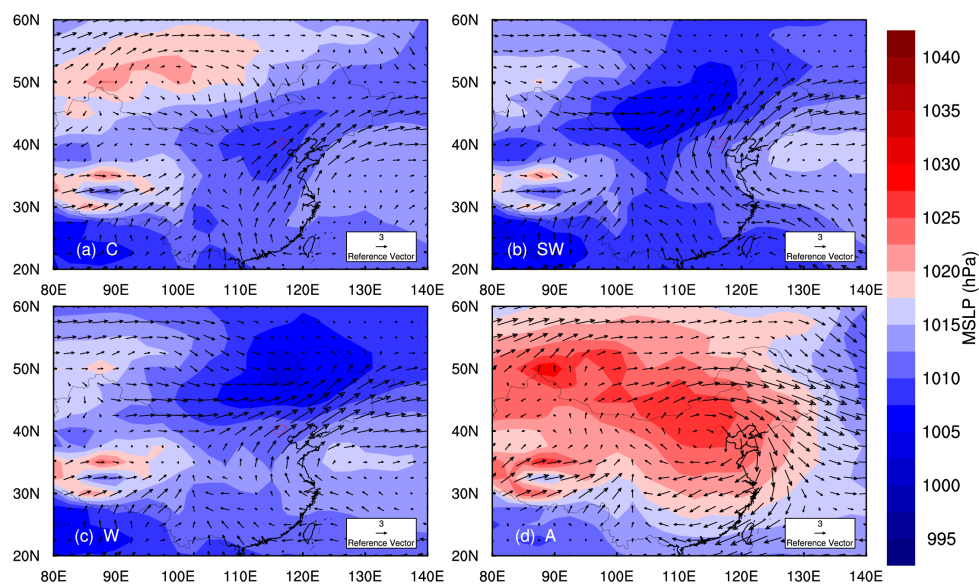
221 As shown in Fig. 3, the locations of the high and low pressures and the intensity of the wind fields at 925
222 hPa under different circulation patterns were clearly distinct. In type C, Beijing was located in the center of low
223 pressure, and the sea to the east of China was controlled by an anticyclone (Fig. 3a). Southwesterly winds
224 prevailed, flowing northward to Beijing along the periphery of the anticyclone with an average wind speed of 3
225 m/s. In type SW, Beijing lay southeast of the low pressure in Mongolia, and the high pressure over the sea was
226 significantly enhanced compared with type C (Fig. 3b). Therefore, southeasterly winds prevailed to the south of
227 Beijing and shifted southwesterly after flowing by. In type W, westerly winds were dominant and converged with
228 southwesterly flows to the north of Beijing (Fig. 3c). The mean velocity of environmental flows in type SW and
229 type W was observably larger than that in type C. In general, the mainland was mainly controlled by low pressure
230 with an anticyclone lying over the sea to the east of China in pollution types C, SW and W, and southerly flows
231 dominated at 925 hPa. By contrast, northern China in the clean type A was occupied by high pressure. Beijing was
232 located in the center of high pressure with strong northerly winds in the lower level (Fig. 3d).

233 The pollution intensity is closely related to the large-scale weather circulations. Although the dominant
234 synoptic patterns in different seasons vary greatly, the modulating effects on air pollution of specific circulation
235 types in different seasons are similar (Liao et al., 2017; Li et al., 2020). The spatial distribution of PM2.5 in Beijing
236 under pollution types C, SW, W and clean type A is shown in Fig. 4. Type C had the highest pollution level, with
237 the PM2.5 concentration increasing from 60 $\mu\text{g}/\text{m}^3$ in the northwestern mountainous area to 90 $\mu\text{g}/\text{m}^3$ in the
238 south-central plain area, which was significantly higher than the values for types SW and W. Type A was highly
239 ventilated, with a PM2.5 concentration below 30 $\mu\text{g}/\text{m}^3$ in most areas. Under the influence of semibasin
240 topography surrounded by mountains on three sides (Fig. 1b), the pollution concentrations in all weather types
241 were characterized by a gradual decrease from southeast to northwest in Beijing.



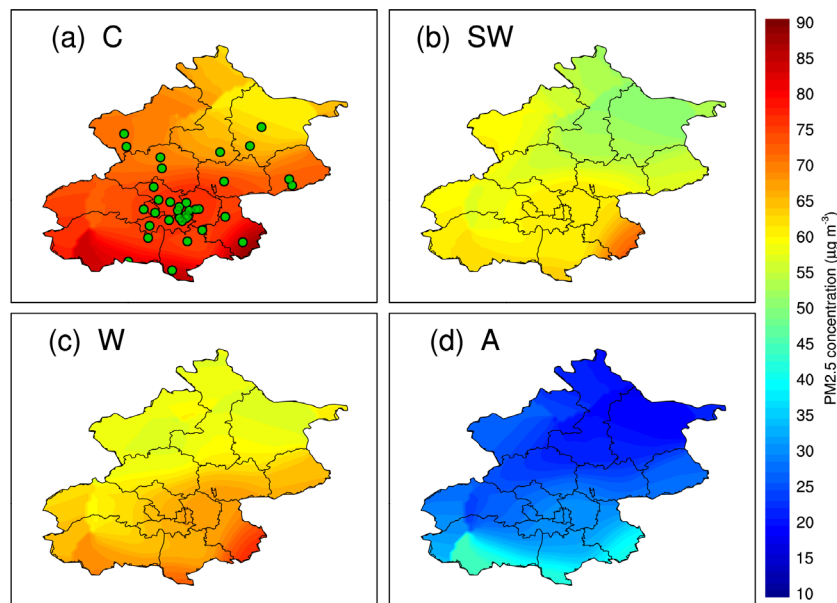
242
243
244
245

Fig. 2 Daily averaged PM_{2.5} concentration in Olympic Center station (box plots, units: $10^{-1} \mu\text{g m}^{-3}$) and the occurrence frequencies of 26 weather types (red dashed lines) from 2018 to 2019. The red boxes represent classical types selected for research. The black dots represent the mean values.



246
247
248

Fig. 3 The daily MSLP (shaded, units: hPa) and wind fields at 925 hPa (vectors, units: m s^{-1}) for types C (a), SW (b), W (c) and A (d) from 2018 to 2019.



249

250 Fig. 4 The averaged PM_{2.5} concentration (shaded, units: $10^{-1} \mu\text{g m}^{-3}$) in Beijing for types C (a), SW (b), W (c) and A
251 (d) from 2018 to 2019. The green dots in Fig. 4a indicate the locations of air quality monitoring sites in Beijing.

252 3.2 The flow field and dynamic-thermal structure of the PBL under typical weather 253 types

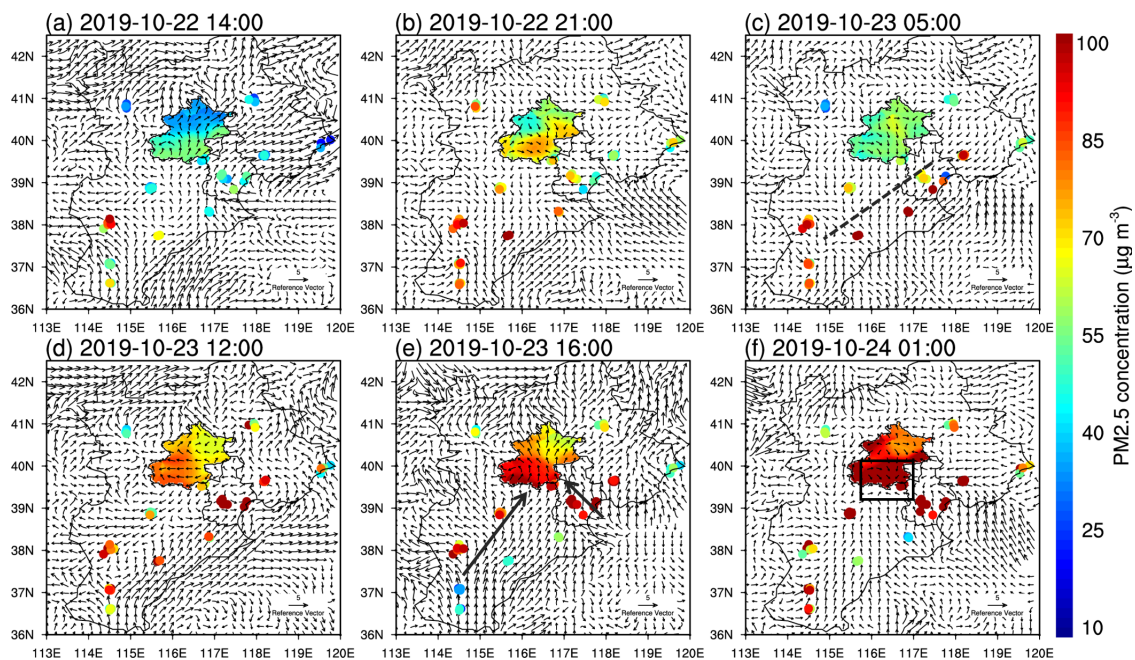
254 As mentioned above, due to the special topography and geographical location in Beijing, both large-scale
255 weather circulations and regional-scale thermal circulations have conspicuous effects on modulating pollution. In
256 addition, the thermal and dynamic structure of the PBL also has an appreciable impact on the mixing and
257 diffusion of pollutants. Therefore, the multiscale circulations can not only influence the pollution directly but also
258 influence it by changing the PBL structure indirectly. To reveal the mechanisms of how the coupling effects of
259 multiscale circulations affect the PBL structure and air pollution under different synoptic patterns, we conduct an
260 analysis of the horizontal flow field and vertical PBL structure in depth by choosing typical cases lasting two days
261 in the same weather type (C, SW, W and A). The typical cases are on October 22 to 24, July 26 to 28, May 15 to 17
262 in 2019 and December 28 to 30 in 2018 respectively.

263 3.2.1 Multilayer PBL structure under type C circulation

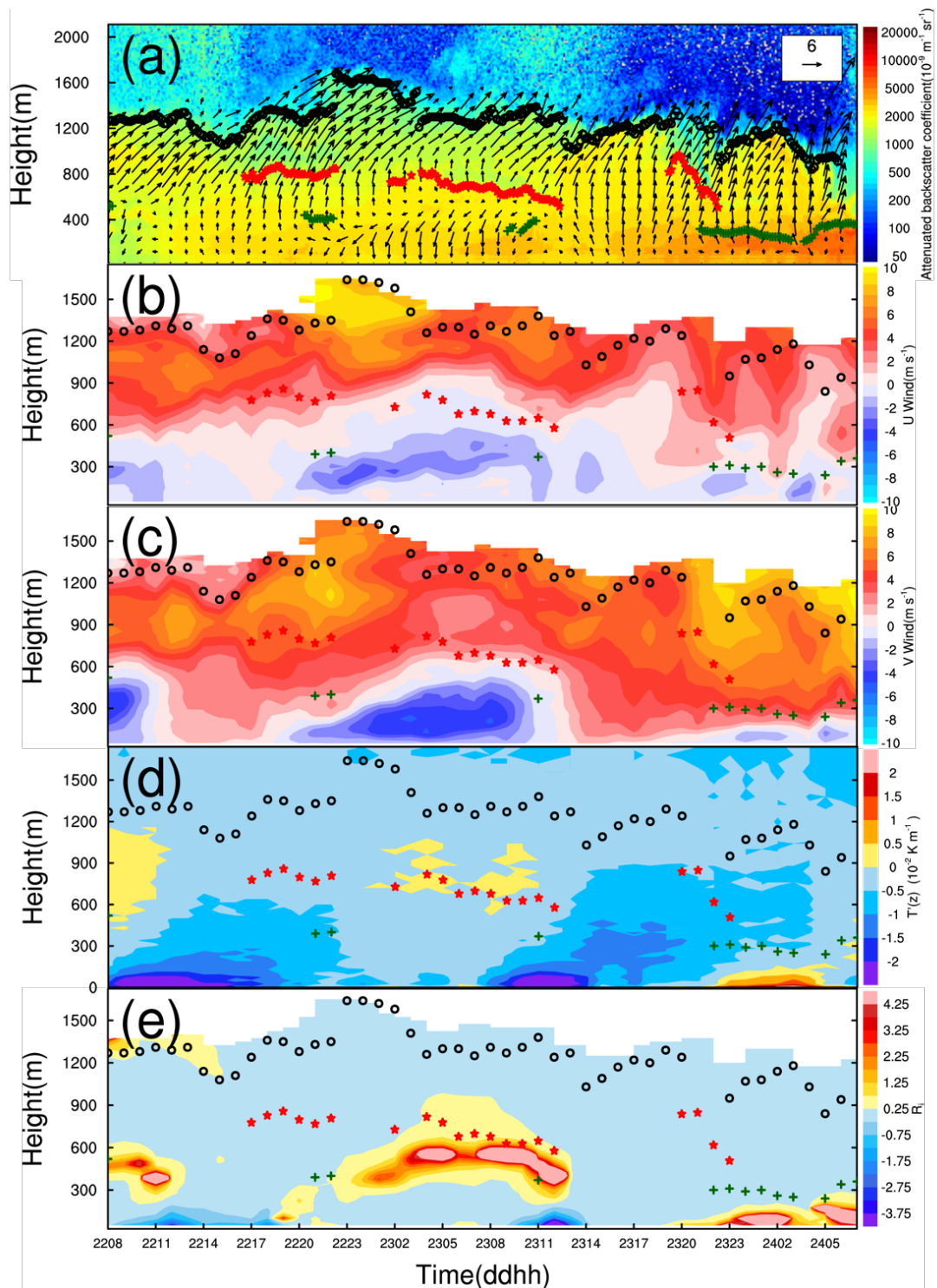
264 The mainland was governed by low pressure under type C synoptic circulations, and the ambient winds
265 were mainly southwesterly (Fig. 3a). On the afternoon of 22nd, the plain breezes in central Hebei, which were
266 induced by thermal contrast between the mountain and plain, blocked weak environmental winds and the direct
267 transportation of pollutants to Beijing (Fig. 5a). The westerly and the northerly mountain breezes began to prevail
268 at night while the conversion from sea breeze to land breeze was not obvious (Fig. 5b). The onshore winds in the
269 coastal area were notably larger than the northerly mountain breezes in southern Chengde (SCD), which were
270 diverted to the west and east. The diverted easterly winds converged with the onshore winds, enhancing the
271 easterly winds and the east pollution transport channel. Sun et al. (2019) have found that the pressure gradients
272 between the plain and mountain areas are critical causes of the easterly winds in Beijing. Consequently, easterly
273 winds gathered with mountain breezes and formed a pollution convergent zone. Weak environmental winds not
274 only made the pollution channels hard to establish but also caused the pollutants to recirculate southward by
275 strong downslope breezes further in the early morning (Fig. 5c). A mesoscale convergent belt was generated in
276 southeastern Hebei, providing conditions for the transportation of pollutants later. At noon on 23rd, the
277 intensified plain winds transported high concentrations of aerosols from the right side of the convergent belt to
278 Beijing (Fig. 5d). Large-scale environmental winds were strengthened and dominated in the afternoon (Fig. 5e),
279 leading to the establishment of the south and east pollution transport channels and further exacerbating the air
280 quality. On the night of 23rd, easterly winds were observably strengthened again, joining with the downslope
281 breezes and the ambient southerly flows (Fig. 5f). The four directional airflows formed a convergent zone that
282 caused pollutants to accumulate dramatically in the plain areas. This convergent region that is generated by the
283 coupling effect of large-scale circulation and regional-scale mountain breezes at night also appeared in other
284 pollution types, as will be discussed later.

285 The PBL under type C circulation presented a multilayer structure without diurnal variation (Fig. 6a). The
286 highly stable structure and weak ambient winds resulted in a higher aerosol concentration near the surface than
287 that in the other pollution types (Fig. 4). The pollution decreased from bottom to top within the PBL and was
288 characterized by a gradient distribution. It is consistent with previous research (Jiang et al., 2021) that the top PBL
289 height is equal to the maximum detection range of wind Lidar. In the daytime, environmental southwesterly
290 winds dominated within the PBL. In the horizontal flow field, zonal winds from Tianjin to the southeast of Beijing
291 turned to be easterly winds and the northerly downslope winds in Beijing were strengthened later on the night of
292 22nd (Fig. 5b, 5c). Inside the PBL, easterly and northerly winds extended to 600 m above the ground from 20 pm
293 on 22nd to 10 am on 23rd (Fig. 6b, 6c), thus the directional shear of meridional and zonal winds increased

294 considerably. The shallower nocturnal PBL coincided with the zero speed zone between the upper environmental
 295 winds and lower regional-scale breezes with the largest directional shear (Fig. 6b, c). Variations of the vertical
 296 dynamic structure in the PBL drove the thermal structure to adjust. Warm air advected by large-scale
 297 southwesterly winds overlay on the cold air advected by regional-scale northeasterly breezes. Consequently, a
 298 conspicuous advective temperature inversion occurred near the shallower nocturnal PBL at 08-09 am on 22nd
 299 and 00-11 am on 23, ranging from 600 m to 900 m above the ground (Fig. 6d). The Richardson number Ri away
 300 from the temperature inversion structure was less than 0.25 (turbulent region) during the night, while it increased
 301 considerably from the periphery of inversion and was larger than 1.0 (stable region) promptly. The sharp jump of
 302 Ri from the turbulent region to the stable region of inversion indicated a vertical stratified structure inside the PBL.
 303 The result suggested that the nocturnal PBL has an inhomogeneous stratification structure characterized by
 304 strong variations of Ri accompanied by inversion structure (Fig. 6e). However, the relatively stronger northerly
 305 breezes compared to the environmental winds made the pollutants recirculate southward horizontally, the wind
 306 shear developed so high that the dynamically stable region was above 300 m and the inversion was above 600 m;
 307 the pollutants dispersed vertically to some extent consequently (Fig. 5c, 6c). Compared to the previous night, the
 308 ambient winds on the night of 23rd were stronger; thus, both south and east transport channels were established,
 309 along with the pollution convergent zone (Fig. 5f). The weak easterly and northerly winds were lower than 300 m
 310 (Fig. 6b, c), resulting in temperature inversion and stable stratification connected to the ground. A high
 311 concentration of pollution was accumulated in the convergent zone horizontally and trapped below the lowest
 312 PBL vertically. Thus, the PM_{2.5} concentration on the night of 23rd was significantly higher than that on 22nd.



313
 314 Fig. 5 The surface winds (vectors, units: $m s^{-1}$) in the NCP and PM_{2.5} concentration in Beijing (shaded, units: $10^{-1} \mu g m^{-3}$), Hebei and Tianjin monitoring sites (scatter, units: $10^{-1} \mu g m^{-3}$) of different times (Local Time) for type C.
 315
 316 The dashed line represents the convergence belt. The arrow lines represent the pollutant transport channels. The
 317 rectangle represents the convergent zone.



318

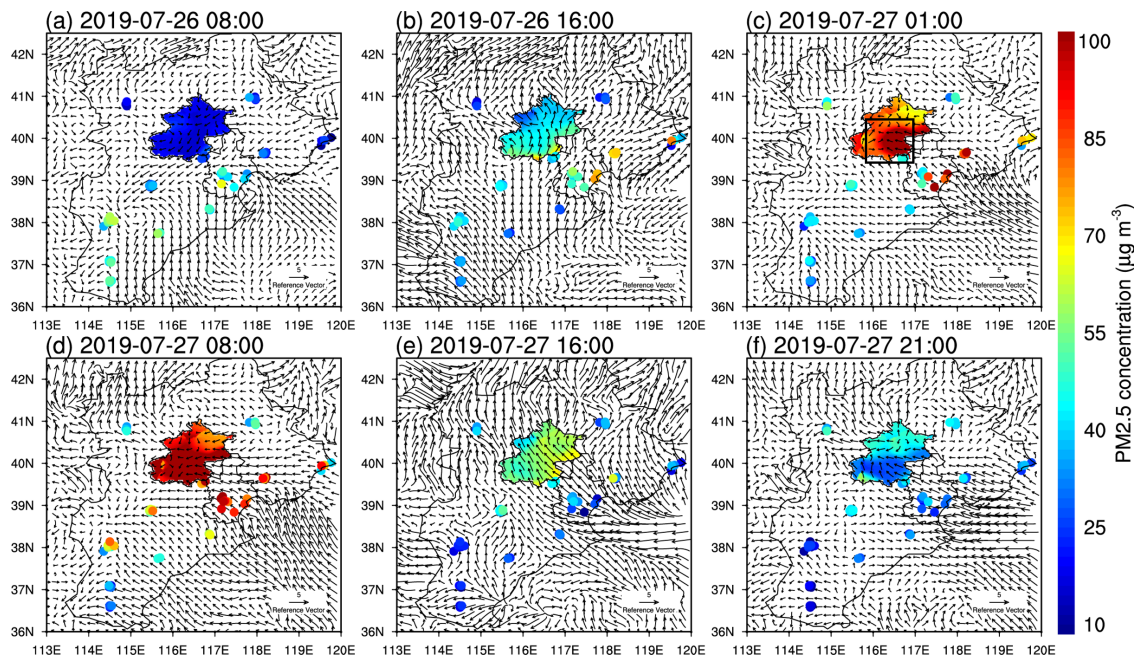
319 Fig. 6 Attenuated backscatter coefficient (shaded, units: $10^{-9} \text{ m}^{-1} \text{ sr}^{-1}$) measured by ceilometer and horizontal
 320 winds (vectors, units: m s^{-1}) measured by Lidar (a), zonal wind component speeds (shaded, units: m s^{-1}) (b),
 321 meridional wind component speeds (shaded, units: m s^{-1}) (c), gradient of temperature $T'(z)$ (shaded, units: K km^{-1})
 322 measured by MWR (d), and Richardson number (shaded) (e) for type C. The green crosses, red stars and black
 323 hollow dots represent the lowest, middle and top PBLH, respectively.

324 3.2.2 Mono-layer PBL structure under type SW circulation

325 Under type SW circulation, the easterly wind component increased in southeastern Hebei and the Bohai Sea,
 326 and the velocity of environmental winds was appreciably higher than that in type C. (Fig. 3b). On the early

327 morning of 26th, mountain breezes carrying clean air masses prevailed in Beijing, and the air quality was good
328 (Fig. 7a). The basic southerly winds dominated in the Beijing-Tianjin-Hebei region in the afternoon, transporting
329 pollutants northward and causing airflow to converge in plain areas (Fig. 7b). However, pollutants were ventilated
330 horizontally by strong ambient winds and diffused vertically by the intensified turbulent mixing within the
331 growing ML, so the aerosol concentration grew slowly during the day (Fig. 8a). At night, the mountain breezes
332 were strengthened while the ambient southerly winds were weakened; hence, the pollutants were transported to
333 Beijing via the east pollution channel (Fig. 7c). Multiscale circulations of different directions joined and generated
334 a convergent zone in the plain area. Afterwards, easterly flows were further strengthened and transported
335 pollutants to Beijing continuously, the severely polluted area moved westward (Fig. 7d, 8a). In the daytime of 27th,
336 the ambient winds prevailed again, and strong ambient winds removed pollutants by enhancing the ventilation
337 and turbulent mixing (Fig. 7e, 8a). Therefore, the PM_{2.5} concentration decreased instantly and the air quality in
338 the Beijing-Tianjin-Hebei region improved markedly (Fig. 7f).

339 Unlike type C, the PBL presented a monolayer structure in type SW, and the aerosol within the PBL was
340 uniformly distributed (Fig. 8a). Furthermore, the PBL had an obvious diurnal variation and the maximum
341 detection distance of wind Lidar was only consistent with the top ML in type SW. The nocturnal PBL and the
342 growing or collapsing ML were usually lower than the maximum detection distance, indicating that there were
343 residual aerosols above the PBL. In the daytime of 26th, southwesterly winds dominated within the PBL, and the
344 temperature lapse rate was greater than 0.5 °C/100 m. Along with radiation reinforcing turbulent kinetic energy,
345 the PBL rose to 1200 m. Pollutants were transported to Beijing but mixed vertically (Fig. 8a), so the PM_{2.5}
346 concentration near the surface grew slowly (Fig. 7b). On the night of 26th, the regional-scale circulation
347 developed upward, and the vertical wind shears between the lower regional breezes and upper environmental
348 winds were strengthened prominently (Fig. 8b, c). The warm advection overlay on the cold advection resulted in
349 advective inversion, forcing the PBL to adjust to become stable (Fig. 8d). Correspondingly, Ri experienced an
350 appreciable increase from the turbulent region above the PBL to the stable region of below the PBL (Fig. 8e). The
351 nocturnal PBL has a homogeneous dynamically stable structure. Similar to type C, a high concentration of
352 pollutants was trapped below the zero wind speed zone where the nocturnal PBL was located. In the daytime of
353 27th, large-scale environmental winds within the PBL were strengthened greatly. The PBL height was 800 m
354 higher than that of the previous day; thus, the pollutants were advected horizontally and diffused vertically (Fig.
355 8a). The basic southerly winds with high speed prevailed in central and southern Beijing on the night of 27th,
356 preventing the mountain winds from flowing southward (Fig. 7f). As a result, no vertical shear of meridional
357 winds occurred in the dynamic field (Fig. 8c) and no temperature inversion occurred in the thermal field (Fig. 8d).
358 The PM_{2.5} concentration was further reduced. It can be inferred that the temperature inversion in type SW was
359 generated by the vertical thermal contrast of meridional winds. When the meridional winds were uniformly
360 southerly winds within and above the PBL, the air masses in the upper layer had the same thermal properties as
361 that in the lower layer, which will reduce the vertical wind shear and destroy the stable inversion structure.



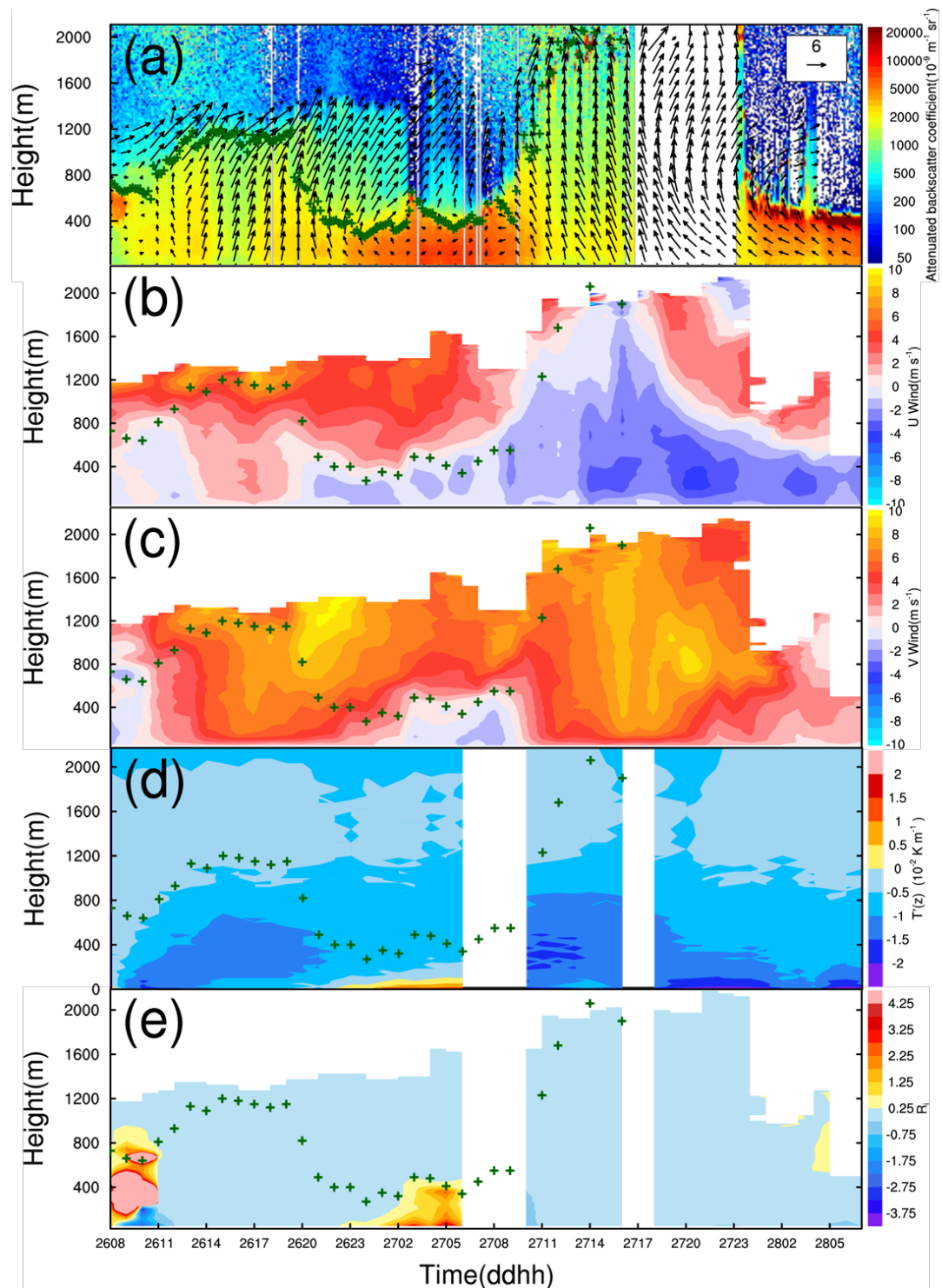
362

363

364

365

Fig. 7 The surface winds (vectors, units: m s^{-1}) in the NCP and PM2.5 concentration in Beijing (shaded, units: $10^{-1} \mu\text{g m}^{-3}$), Hebei and Tianjin monitoring sites (scatter, units: $10^{-1} \mu\text{g m}^{-3}$) of different times (Local Time) for type SW. The rectangle represents the convergent zone.



366

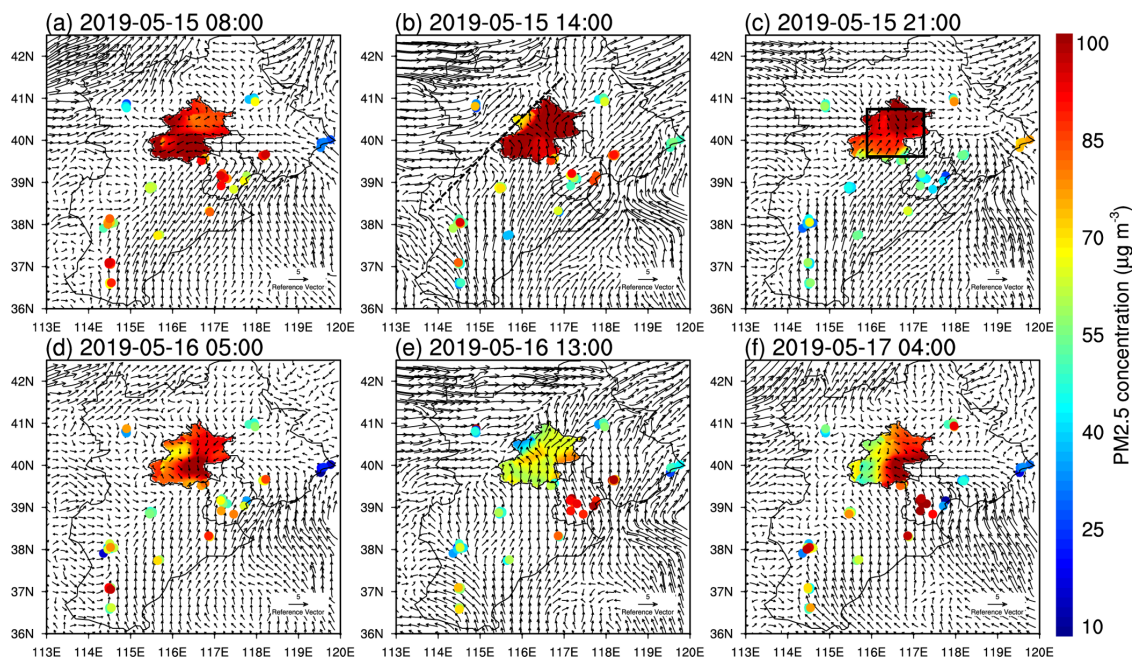
367 Fig. 8 Attenuated backscatter coefficient (shaded, units: $10^{-9} \text{ m}^{-1} \text{ sr}^{-1}$) measured by ceilometer and horizontal
 368 winds (vectors, units: m s^{-1}) measured by Lidar (a), zonal wind component speeds (shaded, units: m s^{-1}) (b),
 369 meridional wind component speeds (shaded, units: m s^{-1}) (c), gradient of temperature $T'(z)$ (shaded, units: K km^{-1})
 370 measured by MWR (d), and Richardson number (shaded) (e) for type SW. The green crosses represent the PBLH.

371 3.2.3 Hybrid structure PBL under type W circulation

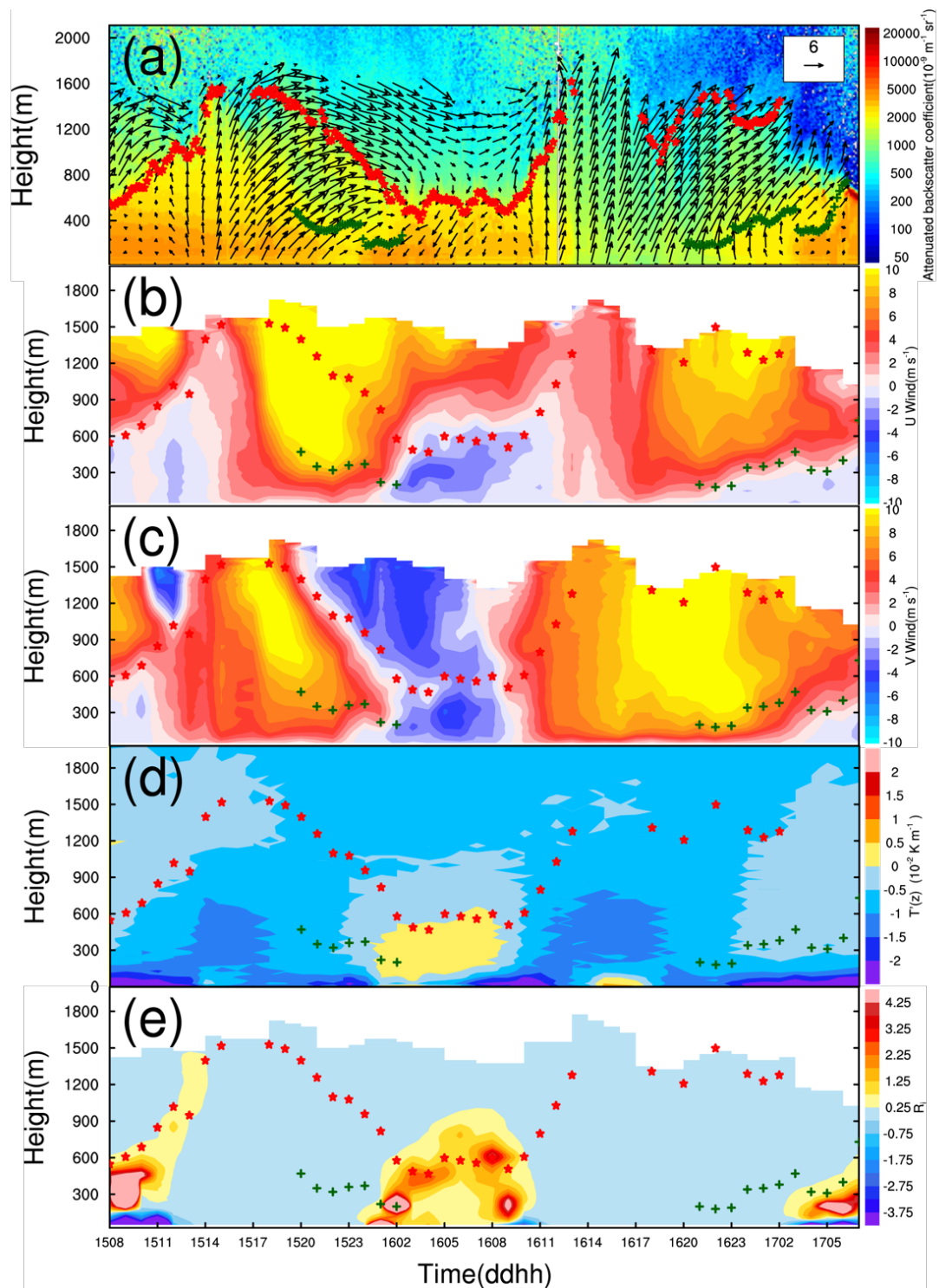
372 Under type W circulation, strong easterly winds transported a high concentration of aerosols to Beijing
 373 through the east pollution channel, and the PM_{2.5} concentration had already reached a high level in the early
 374 morning (Fig. 9a). Taking the mountain as the boundary, environmental westerly winds prevailed in northwestern

375 Hebei and southwesterly winds prevailed in southern Hebei in the afternoon. The two directional flows carried
 376 pollutants and formed a convergent belt along the western mountains (Fig. 3c, 9b). This distribution of synoptic
 377 circulations in type W was conducive to the occurrence of severe pollution around mountains. Similar to other
 378 pollution types, the ambient winds converged with region-scale mountain breezes at night, forming a convergent
 379 zone (Fig. 9c). The convergent zone moved southward later because of intensified mountain breezes (Fig. 9d). The
 380 large velocity of environmental winds leads to strong ventilation (Fig. 9e). In addition, the increasing PBL made
 381 the pollutants diluted vertically, and the air pollution was alleviated temporarily. On night of the 16th (Fig. 9f), the
 382 synergistic effects of multiscale circulations led to the convergent zone again, and pollution occurred in the
 383 easterly flows with a high PM2.5 concentration.

384 The PBL under type W circulation presented a hybrid structure, having similar characteristics of types C and
 385 SW simultaneously. Similar to type C, the aerosol concentration was characterized by a gradient distribution
 386 within the multilayer PBL (Fig. 10a). However, the PBL had an obvious diurnal variation, and the maximum
 387 detection distance of wind Lidar was only consistent with the top ML in the daytime, similar to type SW. Although
 388 the PBL height reached 1600 m in the daytime (Fig. 10a), the PM2.5 concentration at the surface did not decrease
 389 observably because of the massive pollution accumulated previously and the continuous emissions and
 390 transportation of pollutants (Fig. 9b). The mixing layer collapsed along the zero wind speed of meridional winds
 391 after sunset, and the breezes within nocturnal PBL shifted northwesterly at night (Fig. 10b, c). In type W, zonal
 392 circulation dominated. The vertical shear of zonal winds was intensified significantly at night, while the vertical
 393 shear of meridional winds diminished. Therefore, it can be assumed that the temperature inversion in type W was
 394 produced by the vertical shear of zonal winds. The thermal contrast between the upper westerly winds and the
 395 lower easterly winds produced a deep inversion layer that existed from the surface to 500 m (Fig. 10d), as well as
 396 a dynamically stable structure with a depth exceeding 600 m (Fig. 10e). This is consistent with the findings of Hu
 397 et al. (2014) that westerly warm advection from the Loess Plateau was transported over the NCP and imposed a
 398 thermal inversion above the PBL. The top of the PBL was consistent with the top of the inversion and zero wind
 399 speed zone, and a high concentration of aerosols was trapped below the zero wind speed zone.



400
 401 Fig. 9 The surface winds (vectors, units: m s^{-1}) in the NCP and PM2.5 concentration in Beijing (shaded, units: 10^{-1}
 402 $\mu\text{g m}^{-3}$), Hebei and Tianjin monitoring sites (scatter, units: $10^{-1} \mu\text{g m}^{-3}$) of different times (Local Time) for type W.
 403 The dashed line represents the convergence belt. The rectangle represents the convergent zone.



404

405 Fig. 10 Attenuated backscatter coefficient (shaded, units: $10^{-9} \text{ m}^{-1} \text{ sr}^{-1}$) measured by ceilometer and horizontal
 406 winds (vectors, units: m s^{-1}) measured by Lidar (a), zonal wind component speeds (shaded, units: m s^{-1}) (b),
 407 meridional wind component speeds (shaded, units: m s^{-1}) (c), gradient of temperature $T'(z)$ (shaded, units: K km^{-1})
 408 measured by MWR (d), and Richardson number (shaded) (e) for type W. The green crosses and red stars represent
 409 the low and top PBLH, respectively.

410 3.2.4 Strong turbulent PBL structure under clean type A circulation

411 Strikingly different from the circulations of pollution types, the mainland was under high pressure control in
 412 the clean type, and northwesterly winds with a high velocity carrying clean air masses moved southward (Fig.

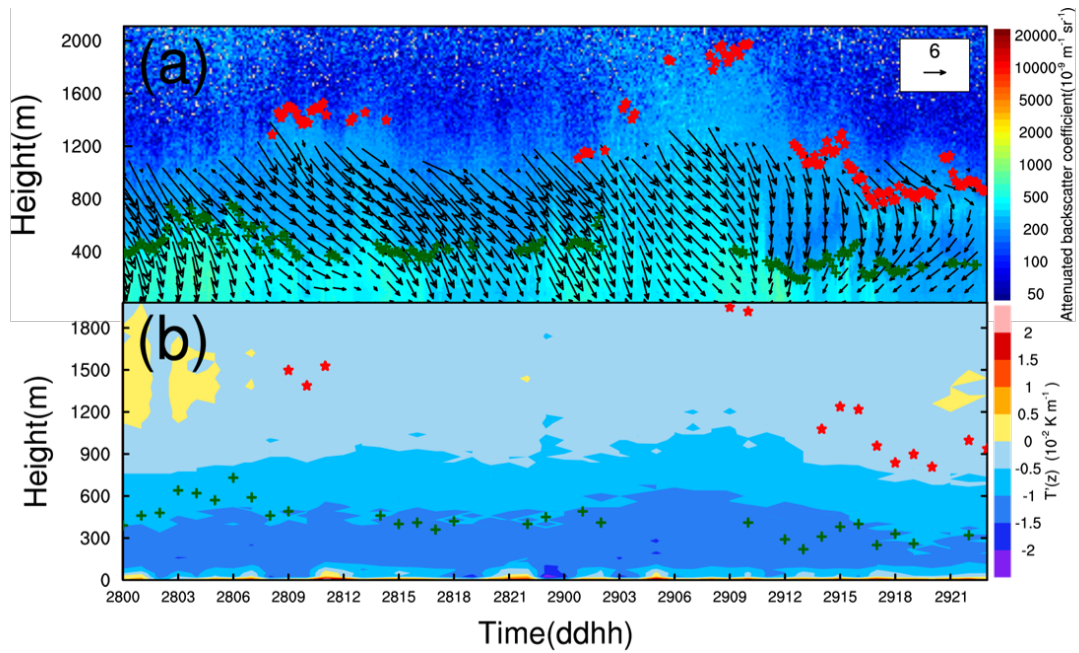
413 11a). Strong winds were favorable for the turbulent mixing and the vertical dispersion of pollutants. In addition,
414 the strong ventilation was beneficial to the horizontal spreading of pollutants. Due to the intense turbulent
415 mixing, the vertical wind shear and the diurnal variation of thermal field disappear, and there is no distinct PBL
416 structure different from the free atmosphere (Fig. 11a, b). The lapse rate of temperature was greater than
417 $1\text{ }^{\circ}\text{C}/100\text{ m}$, and Ri was less than 0.25 within the PBL (not shown). Although the aerosol concentration of the clean
418 type was far less than that of pollution types, the PBL height was only 500 m at night (Fig. 11a). Sometimes, the
419 PBL in the clean type was even lower than that of pollution types, or extended to 2-3 km swiftly because of the
420 instant upward diffusion of aerosol particulates. Unlike pollution types, the PBL height is inconsistent with the
421 maximum detection range of wind Lidar. Therefore, different circulation types should be distinguished when
422 analyzing the long-term relationships between the PBL height and pollution concentration. As shown in Fig. 12 c
423 and d, under the governing of high pressure, descending and divergent airflows of the clean type dominated the
424 whole lower and middle parts of the troposphere, and the sinking velocity was significantly higher than that of
425 pollution types. The vertical velocity changed little vertically due to the northerly winds with a large speed
426 penetrating downward. The intensity of sinking and divergence was higher at night than that in the day, with the
427 strongest divergence occurring near the surface.

428 3.3 Multiscale circulations coupling mechanism for air pollution

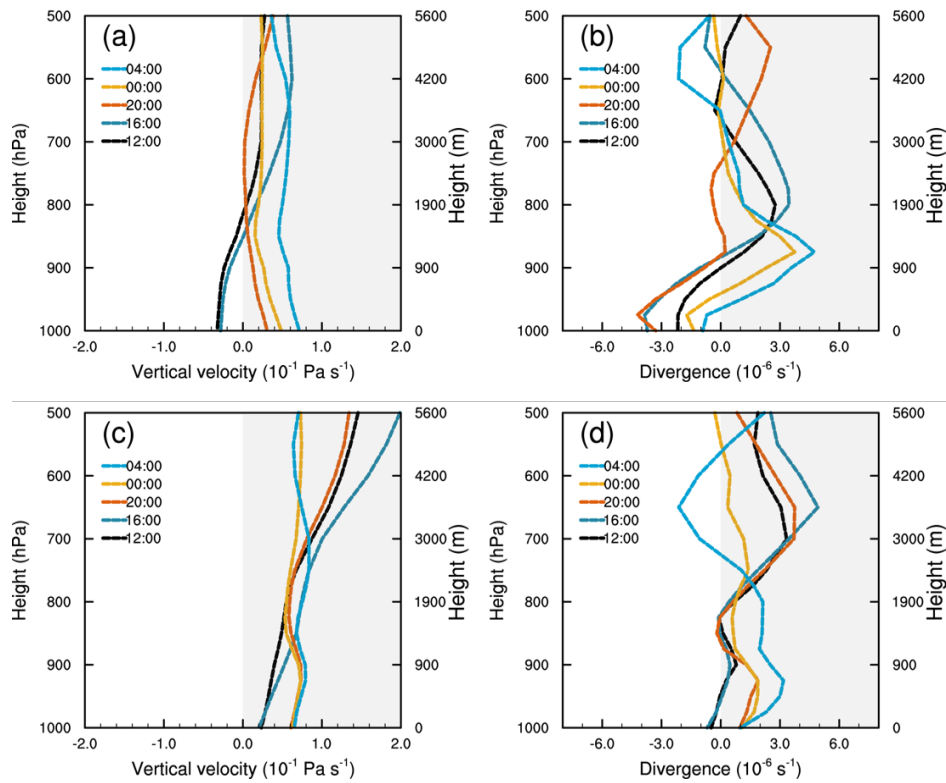
429 In addition to horizontal circulations, the vertical motion of basic airflows is also a crucial dynamic factor in
430 forming stable structure during pollution episodes. The pollution types shared similar vertical motion
431 characteristics as shown in Fig. 12. The basic flows at the bottom of the troposphere is convergence and the flows
432 above it is divergence at all times of a day (Fig. 12b). In the daytime, the environmental southerly winds were
433 obstructed on three sides by mountains. Airflows slowed down or stagnated in the plain areas, forming the
434 topographic convergence. While at night the convergence was caused by the joint of environmental winds and
435 regional breezes, and the height of convergence zone reduced simultaneously with the nocturnal PBL because the
436 regional circulations developed below the shallower nocturnal PBL. Unlike the divergence field, the vertical
437 velocity in the daytime differed from that in the nighttime because of the diurnal variations of PBL structure (Fig.
438 12a). In the daytime, the thermodynamic convection and the wind speed were enhanced expressively (Fig. 8a,
439 10a), thus the intensified turbulence will help the flows to move upward and cause the pollutants close to the
440 ground to mix vertically within the PBL to some extent. However, the sinking and divergent flows superposed
441 above the PBL, preventing the pollutants from moving upward continuously and making it difficult for the aerosol
442 particulates to diffuse beyond. As a consequence, the pollutants accumulate slowly in the daytime because of the
443 common influences of horizontal topographic blocking and vertical upward mixing with the increasing PBL.
444 However in nighttime, as the thermodynamic convection weakened and the inversion structure formed, it turned
445 to be sinking movement at the bottom of the troposphere when the cold northerly regional breezes prevailed.
446 Wu et al. (2017) found that the descending motion of synoptic circulations contributed to a reduction in the PBLH
447 by compressing the air mass. Therefore, massive pollutants were capped near the surface and accumulated
448 rapidly at night under the convergent sinking motion accompanied by temperature inversion structure.

449 To sum up, different pollution patterns (C, SW and W) have similar influential mechanisms that both
450 horizontal and vertical coupling effects of the multiscale circulations have contributed to air pollution. The
451 horizontal coupling mechanism is shown in Fig. 1b. The environmental winds transport pollutants emitted from
452 southern sources to Beijing, mainly through south and east pollution channels. Large-scale environmental winds
453 and regional-scale breezes are coupled, generating a convergent zone of four directional flows horizontally and
454 aggravating the air pollution directly at night. The relative strength of winds makes the severely polluted area
455 move around horizontally from 39°N to 41°N . The schematic of Fig. 13 demonstrates that the vertical coupling
456 mechanism further influences the mixing and dispersion of pollution indirectly by changing the PBL structure. In

457 the daytime, the sinking divergent flows overlaying the rising convergent flows within the PBL inhibit the
 458 continuous upward dispersion of pollutants. At night, the warm advection transported by the upper
 459 environmental winds overlays the cold advection transported by the lower regional breezes, generating strong
 460 directional wind shear and advective inversion, which are near the top of regional breezes. This dynamic structure
 461 forces the PBL to be a stable stratification. The nocturnal PBL is located at the zero speed zone between the
 462 regional-scale breezes and the environmental winds, and the relative strength of winds determines the PBL height.
 463 The capping inversion cooperating with the convergent sinking motion within the PBL suppresses massive
 464 pollutants below the zero speed zone.



465
 466 Fig. 11 Attenuated backscatter coefficient (shaded, units: $10^{-9} \text{ m}^{-1} \text{ sr}^{-1}$) measured by ceilometer and horizontal
 467 winds (vectors, units: m s^{-1}) measured by Lidar (a), and gradient of temperature $T'(z)$ (shaded, units: K km^{-1})
 468 measured by MWR (b) for type A. The green crosses and red stars represent the low and top PBLH, respectively.

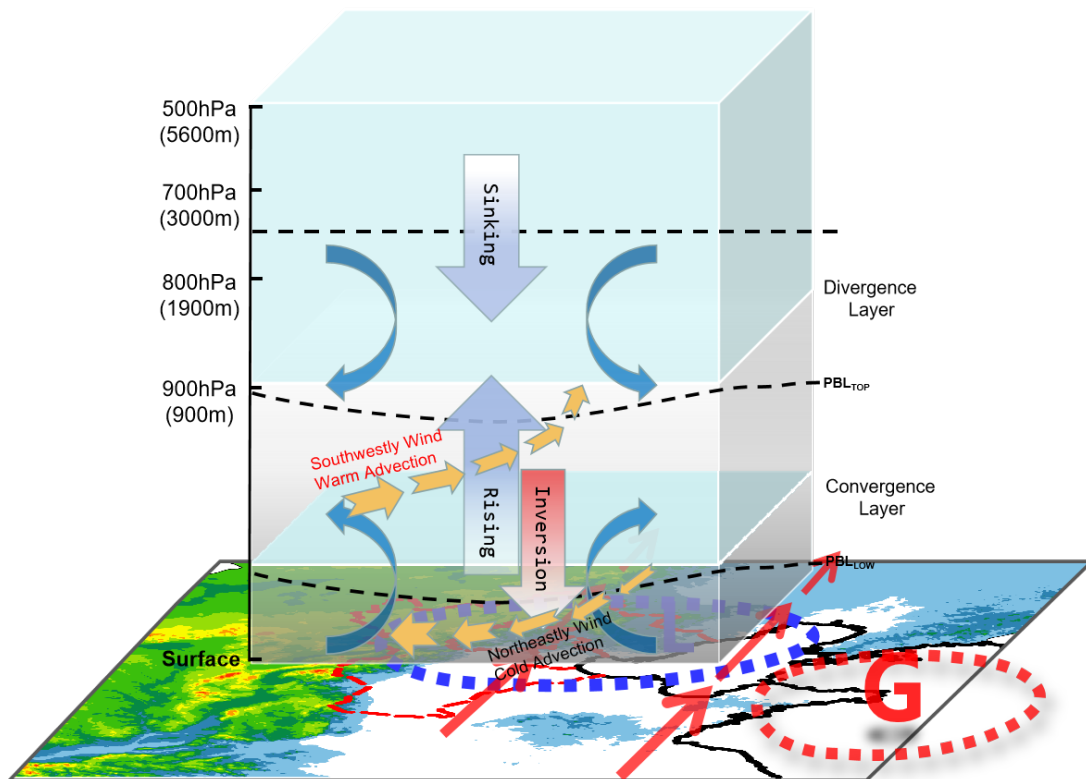


469

470 Fig. 12 The averaged vertical velocity (units: Pa s^{-1} , negative (positive) value denotes updraft (downward)

471 movement) (a, c) and divergence (units: 10^{-5} s^{-1}) (b, d) of pollution types (a, b) and the clean type (c, d) in the

472 North China Plain



473

474 Fig. 13 The schematic of vertical coupling mechanism of multiscale circulations for typical pollution types; The

475 horizontal part is the background circulations of MSLP. The vertical part is the PBL dynamic-thermal structure over

476 the NCP region

477 4. Conclusions and Discussion

478 This paper explores the direct regulatory effect and indirect coupling effect of synoptic circulations by
479 choosing the most frequent pollution types and clean type classified by LWT approach. The PBL dynamic-thermal
480 structure and the severe pollution area under typical circulations types are further investigated. Results suggest
481 that different pollution patterns have similar influential mechanisms on PBL structure and air pollution. The direct
482 regulatory effect of synoptic circulations plays a leading role in the daytime, large-scale southerly winds dominate
483 and are favorable for the pollution transport to NCP region and the accumulation in front of mountains in the
484 early stage of pollution. However during the period of pollution, the relative stronger southerly winds and the
485 increasing PBL height are adverse to the accumulation of pollutants, or even make pollutants ventilated
486 horizontally and diluted vertically. While the indirect effect played a leading role in the nighttime by coupling
487 mechanisms. The coexisting multiscale circulations at night, on the one hand, affect the pollution via the
488 horizontal coupling effect, which produces a pollution convergent zone of different direction winds. The relative
489 strength of winds makes the polluted area move around horizontally between 39°N and 41°N. On the other hand,
490 the multiscale circulations regulate the mixing and diffusion of pollutants by the vertical coupling effect, which
491 changes the PBL dynamic and thermal structure. Vertical shear between the ambient winds and regional-scale
492 breezes leads to advective inversion structure with strong variations of R_i . The nocturnal shallower PBL is
493 consistent with the zero velocity zone, where massive pollutants were suppressed below, and the relative
494 strength of winds determines the PBL height.

495 The multilayer PBL under type C circulation has no diurnal variation. Weak ambient winds strengthen the
496 mountain breezes observably at night, as a result the vertical shear and temperature inversion can reach 600m
497 and 900 m respectively. An inhomogeneous stratification with sharp jump of R_i is formed from the periphery of
498 inversion. The severe polluted area was located to the south of Beijing. The mono-layer PBL under southwesterly
499 circulation with obvious diurnal variation can reach 2000 m in the daytime. Strong environmental winds restrain
500 the development of regional breezes at night, the zero speed zone is located at 400 m and the inversion
501 generated by the vertical shear of meridional winds is lower than 200 m. Southerly winds within and above the
502 PBL having the same thermal properties will diminish the vertical shear and damage the advective inversion
503 structure. The PBL under westerly circulation has a hybrid structure with both multiple aerosol layers and diurnal
504 variation. The inversion is generated by the vertical shear of zonal winds. The polluted areas under southwesterly
505 and westerly circulations are located more northerly. Clean and strong north winds are dominated under
506 anticyclone circulation, the vertical shear and the diurnal variation of thermal field disappear and there is no
507 distinct PBL structure.

508 This study suggests that synoptic-scale circulations or the regional-scale circulations don't influence the PBL
509 structure and air pollution separately but by the synergistic ways instead. The new knowledge of the coupling
510 mechanism of multiscale circulations has appreciable implications for deepening the understanding of
511 cooperation of influential factors in severe pollution processes in the background of unique topography. The new
512 findings about the PBL dynamic-thermal structure and the distribution of pollution provide a reference for
513 forecasting the severe pollution area under the most frequent synoptic circulation types in Beijing. Although the
514 essential impacts of synoptic-scale and regional-scale circulations on PBL dynamic-thermal structure are
515 emphasized in the paper, the feedback impact of aerosols should not be neglect either when investigating the PBL
516 structure and air pollution.

517 Data availability

518 The hourly ground level PM_{2.5} concentration data can be obtained from the National Urban Air Quality

519 Real-time Publishing Platform (<http://106.37.208.233:20035/>). Other data used in this study can be acquired upon
520 request to the corresponding author.

521 Competing interests

522 The authors declare that they have no known competing financial interests or personal relationships that
523 could have appeared to influence the work reported in this paper.

524 Author contribution

525 XJ designed the study. JY, WY, TG, JD, ZD, WM, DL WL, WT, WF contributed to observation data, provided
526 experimental assistance and analyzed methodology. JY and XJ wrote the paper with inputs from all the other
527 authors.

528 Acknowledgments

529 This study was supported by the National Key Research and Development Program of China (grant number
530 2016YFC0202001) and the Chinese Academy of Sciences Strategic Priority Research Program (XDA23020301).

531 References

- 532 Aitken, M. L., Rhodes, M. E., and Lundquist, J. K.: Performance of a Wind-Profiling Lidar in the Region of Wind
533 Turbine Rotor Disks, *Journal of Atmospheric and Oceanic Technology*, 29, 347-355, 2012.
- 534 Banakh, V. A., Smalikho, I. N., and Falits, A. V.: Wind-Temperature Regime and Wind Turbulence in a Stable
535 Boundary Layer of the Atmosphere: Case Study, *Remote Sensing*, 12, 955, 2020.
- 536 Bei, N., Zhao, L., Wu, J., Li, X., Feng, T., and Li, G.: Impacts of sea-land and mountain-valley circulations on the air
537 pollution in Beijing-Tianjin-Hebei (BTH): A case study, *Environmental Pollution*, 234, 429-438, 2018.
- 538 Chen, Y., Zhao, C., Zhang, Q., Deng, Z., Huang, M., and Ma, X.: Aircraft study of Mountain Chimney Effect of Beijing,
539 China, *Journal of Geophysical Research-Atmospheres*, 114, 2009.
- 540 Cheng, Z., Luo, L., Wang, S., Wang, Y., Sharma, S., Shimadera, H., Wang, X., Bressi, M., de Miranda, R. M., Jiang, J.,
541 Zhou, W., Fajardo, O., Yan, N., and Hao, J.: Status and characteristics of ambient PM_{2.5} pollution in global
542 megacities, *Environment International*, 89-90, 212-221, 2016.
- 543 Dai, L., Xin, J., Zuo, H., Ma, Y., Zhang, L., Wu, X., Ma, Y., Jia, D., and Wu, F.: Multilevel Validation of Doppler Wind
544 Lidar by the 325 m Meteorological Tower in the Planetary Boundary Layer of Beijing, *Atmosphere*, 11, 1051,
545 2020.
- 546 Ding, A. J., Huang, X., Nie, W., Sun, J. N., Kerminen, V. M., Petaja, T., Su, H., Cheng, Y. F., Yang, X. Q., Wang, M. H.,
547 Chi, X. G., Wang, J. P., Virkkula, A., Guo, W. D., Yuan, J., Wang, S. Y., Zhang, R. J., Wu, Y. F., Song, Y., Zhu, T.,
548 Zilitinkevich, S., Kulmala, M., and Fu, C. B.: Enhanced haze pollution by black carbon in megacities in China,
549 *Geophysical Research Letters*, 43, 2873-2879, 2016.
- 550 Fu, G. Q., Xu, W. Y., Yang, R. F., Li, J. B., and Zhao, C. S.: The distribution and trends of fog and haze in the North
551 China Plain over the past 30 years, *Atmospheric Chemistry and Physics*, 14, 11949-11958, 2014.
- 552 Gryning, S.-E., Floors, R., Pena, A., Batchvarova, E., and Bruemmer, B.: Weibull Wind-Speed Distribution
553 Parameters Derived from a Combination of Wind-Lidar and Tall-Mast Measurements Over Land, Coastal and
554 Marine Sites, *Boundary-Layer Meteorology*, 159, 329-348, 2016.
- 555 Hu, X.-M., Ma, Z., Lin, W., Zhang, H., Hu, J., Wang, Y., Xu, X., Fuentes, J. D., and Xue, M.: Impact of the Loess
556 Plateau on the atmospheric boundary layer structure and air quality in the North China Plain: A case study,
557 *Science of the Total Environment*, 499, 228-237, 2014.
- 558 Huang, M., Gao, Z., Miao, S., and Xu, X.: Characteristics of sea breezes over the Jiangsu coastal area, China,

559 International Journal of Climatology, 36, 3908-3916, 2016.

560 Jenkinson, A. F., and Collison, F. P.: An initial climatology of gales over the North Sea, Synoptic climatology branch
561 memorandum, 62, 18, 1977.

562 Jiang, Y., Xin, J., Zhao, D., Jia, D., Tang, G., Quan, J., Wang, M., and Dai, L.: Analysis of differences between
563 thermodynamic and material boundary layer structure: Comparison of detection by ceilometer and
564 microwave radiometer, Atmospheric Research, 248, 105179, 2021.

565 Kotthaus, S., and Grimmond, C. S. B.: Atmospheric boundary-layer characteristics from ceilometer measurements.
566 Part 1: A new method to track mixed layer height and classify clouds, Quarterly Journal of the Royal
567 Meteorological Society, 144, 1525-1538, 2018.

568 Lamb, H. H., and Hh, L.: British Isles weather types and a register of the daily sequence of circulation patterns
569 1861-1971, 1972.

570 Leung, D. M., Tai, A. P., Mickley, L. J., Moch, J. M., Donkelaar, A. V., Shen, L., and Martin, R. V.: Synoptic
571 meteorological modes of variability for fine particulate matter (PM_{2.5}) air quality in major metropolitan
572 regions of China, Atmospheric Chemistry and Physics, 18, 6733-6748, 2018.

573 Li, L.-j., Ying, W., Zhang, Q., Tong, Y. U., Yue, Z., and Jun, J. I. N.: Spatial distribution of aerosol pollution based on
574 MODIS data over Beijing, China, Journal of Environmental Sciences, 19, 955-960, 2007.

575 Li, M., Wang, L., Liu, J., Gao, W., Song, T., Sun, Y., Li, L., Li, X., Wang, Y., Liu, L., Daellenbach, K. R., Paasonen, P. J.,
576 Kerminen, V.-M., Kulmala, M., and Wang, Y.: Exploring the regional pollution characteristics and
577 meteorological formation mechanism of PM_{2.5} in North China during 2013-2017, Environment International,
578 134, 105283, 2020.

579 Li, X., Ma, Y., Wei, W., Zhang, Y., Liu, N., Hong, Y., and Wang, Y.: Vertical Distribution of Particulate Matter and its
580 Relationship with Planetary Boundary Layer Structure in Shenyang, Northeast China, Aerosol and Air Quality
581 Research, 19, 2464-2476, 2019.

582 Li, Z., Guo, J., Ding, A., Liao, H., Liu, J., Sun, Y., Wang, T., Xue, H., Zhang, H., and Zhu, B.: Aerosol and
583 boundary-layer interactions and impact on air quality, National Science Review, 4, 810-833, 2017.

584 Liao, Z., Gao, M., Sun, J., and Fan, S.: The impact of synoptic circulation on air quality and pollution-related human
585 health in the Yangtze River Delta region, Science of the Total Environment, 607, 838-846, 2017.

586 Liu, S., Liu, Z., Li, J., Wang, Y., Ma, Y., Sheng, L., Liu, H., Liang, F., Xin, G., and Wang, J.: Numerical simulation for the
587 coupling effect of local atmospheric circulations over the area of Beijing, Tianjin and Hebei Province, Science
588 in China Series D-Earth Sciences, 52, 382-392, 2009.

589 Liu, Y., Wang, B., Zhu, Q., Luo, R., Wu, C., and Jia, R.: Dominant Synoptic Patterns and Their Relationships with PM
590 2.5 Pollution in Winter over the Beijing-Tianjin-Hebei and Yangtze River Delta Regions in China, Journal of
591 Meteorological Research, 33, 765-776, 2019.

592 Lou, M., Guo, J., Wang, L., Xu, H., Chen, D., Miao, Y., Lv, Y., Li, Y., Guo, X., Ma, S., and Li, J.: On the Relationship
593 Between Aerosol and Boundary Layer Height in Summer in China Under Different Thermodynamic
594 Conditions, Earth and Space Science, 6, 887-901, 2019.

595 Miao, Y., Guo, J., Liu, S., Liu, H., Li, Z., Zhang, W., and Zhai, P.: Classification of summertime synoptic patterns in
596 Beijing and their associations with boundary layer structure affecting aerosol pollution, Atmospheric
597 Chemistry and Physics, 17, 3097-3110, 2017.

598 Miao, Y., Hu, X.-M., Liu, S., Qian, T., Xue, M., Zheng, Y., and Wang, S.: Seasonal variation of local atmospheric
599 circulations and boundary layer structure in the Beijing-Tianjin-Hebei region and implications for air quality,
600 Journal of Advances in Modeling Earth Systems, 7, 1602-1626, 2015a.

601 Miao, Y., Liu, S., Zheng, Y., Wang, S., Chen, B., Zheng, H., and Zhao, J.: Numerical study of the effects of local
602 atmospheric circulations on a pollution event over Beijing-Tianjin-Hebei, China, Journal of Environmental

603 Sciences, 30, 9-20, 2015b.

604 Muenkel, C., Eresmaa, N., Rasanen, J., and Karppinen, A.: Retrieval of mixing height and dust concentration with
605 lidar ceilometer, *Boundary-Layer Meteorology*, 124, 117-128, 2007.

606 O'Connor, E. J., Illingworth, A. J., Brooks, I. M., Westbrook, C. D., Hogan, R. J., Davies, F., and Brooks, B. J.: A
607 Method for Estimating the Turbulent Kinetic Energy Dissipation Rate from a Vertically Pointing Doppler Lidar,
608 and Independent Evaluation from Balloon-Borne In Situ Measurements, *Journal of Atmospheric and Oceanic
609 Technology*, 27, 1652-1664, 2010.

610 Petaja, T., Jarvi, L., Kerminen, V. M., Ding, A. J., Sun, J. N., Nie, W., Kujansuu, J., Virkkula, A., Yang, X. Q., Fu, C. B.,
611 Zilitinkevich, S., and Kulmala, M.: Enhanced air pollution via aerosol-boundary layer feedback in China,
612 *Scientific Reports*, 6, 18998, 2016.

613 Quan, J., Tie, X., Zhang, Q., Liu, Q., Li, X., Gao, Y., and Zhao, D.: Characteristics of heavy aerosol pollution during
614 the 2012-2013 winter in Beijing, China, *Atmospheric Environment*, 88, 83-89, 2014.

615 Song, C., Wu, L., Xie, Y., He, J., Chen, X., Wang, T., Lin, Y., Jin, T., Wang, A., and Liu, Y.: Air pollution in China: Status
616 and spatiotemporal variations, *Environmental pollution*, 227, 334-347, 2017.

617 Steyn, D. G., Baldi, M., and Hoff, R. M.: The detection of mixed layer depth and entrainment zone thickness from
618 lidar backscatter profiles, *Journal of Atmospheric and Oceanic Technology*, 16, 953-959, 1999.

619 Stull, R. B.: *An Introduction to Boundary Layer Meteorology*, Kluwer Academic Publishers, Dordrecht, 1988.

620 Sun, Z.-b., Wang, H., Guo, C., Wu, J., Cheng, T., and Li, Z.-m.: Barrier effect of terrain on cold air and return flow of
621 dust air masses, *Atmospheric Research*, 220, 81-91, 2019.

622 Suomi, I., Gryning, S.-E., O'Connor, E. J., and Vihma, T.: Methodology for obtaining wind gusts using Doppler lidar,
623 *Quarterly Journal of the Royal Meteorological Society*, 143, 2061-2072, 2017.

624 Tai, A. P. K., Mickley, L. J., and Jacob, D. J.: Correlations between fine particulate matter (PM_{2.5}) and
625 meteorological variables in the United States: Implications for the sensitivity of PM_{2.5} to climate change,
626 *Atmospheric Environment*, 44, 3976-3984, 2010.

627 Tang, G., Zhu, X., Hu, B., Xin, J., Wang, L., Muenkel, C., Mao, G., and Wang, Y.: Impact of emission controls on air
628 quality in Beijing during APEC 2014: lidar ceilometer observations, *Atmospheric Chemistry and Physics*, 15,
629 12667-12680, 2015.

630 Trigo, R. M., and DaCamara, C. C.: Circulation weather types and their influence on the precipitation regime in
631 Portugal, *International Journal of Climatology*, 20, 1559-1581, 2000.

632 Tsaknakis, G., Papayannis, A., Kokkalis, P., Amiridis, V., Kambezidis, H. D., Mamouri, R. E., Georgoussis, G., and
633 Avdikos, G.: Inter-comparison of lidar and ceilometer retrievals for aerosol and Planetary Boundary Layer
634 profiling over Athens, Greece, *Atmospheric Measurement Techniques*, 4, 1261-1273, 2011.

635 Wang, X., Dickinson, R. E., Su, L., Zhou, C., and Wang, K.: PM_{2.5} POLLUTION IN CHINA AND HOW IT HAS BEEN
636 EXACERBATED BY TERRAIN AND METEOROLOGICAL CONDITIONS, *Bulletin of the American Meteorological
637 Society*, 99, 105-120, 2018.

638 Wu, P., Ding, Y., and Liu, Y.: Atmospheric circulation and dynamic mechanism for persistent haze events in the
639 Beijing-Tianjin-Hebei region, *Advances in Atmospheric Sciences*, 34, 429-440, 2017.

640 Xu, T., Song, Y., Liu, M., Cai, X., Zhang, H., Guo, J., and Zhu, T.: Temperature inversions in severe polluted days
641 derived from radiosonde data in North China from 2011 to 2016, *Science of the Total Environment*, 647,
642 1011-1020, 2019.

643 Ye, X., Song, Y., Cai, X., and Zhang, H.: Study on the synoptic flow patterns and boundary layer process of the
644 severe haze events over the North China Plain in January 2013, *Atmospheric Environment*, 124, 129-145,
645 2016.

646 Yu, B., Zhu, B., Dou, J., Zhang, W., and Hu, D.: Classification of air pollution synoptic patterns and air pollutants

647 transport/purification effect by cold front over Hangzhou, *China Environmental Science*, 37, 452-459, 2017.

648 Zhang, R.: Warming boosts air pollution, *Nature Climate Change*, 7, 238-239, 2017.

649 Zhang, Y., Ding, A., Mao, H., Nie, W., Zhou, D., Liu, L., Huang, X., and Fu, C.: Impact of synoptic weather patterns
650 and inter-decadal climate variability on air quality in the North China Plain during 1980-2013, *Atmospheric
651 Environment*, 124, 119-128, 2016.

652 Zhang, Y., Guo, J., Yang, Y., Wang, Y., and Yin, S. H. L.: Vertical Wind Shear Modulates Particulate Matter Pollutions:
653 A Perspective from Radar Wind Profiler Observations in Beijing, China, *Remote Sensing*, 12, 546, 2020.

654 Zhao, D., Xin, J., Gong, C., Quan, J., Liu, G., Zhao, W., Wang, Y., Liu, Z., and Song, T.: The formation mechanism of
655 air pollution episodes in Beijing city: Insights into the measured feedback between aerosol radiative forcing
656 and the atmospheric boundary layer stability, *Science of the Total Environment*, 692, 371-381, 2019.

657 Zheng, X. Y., Fu, Y. F., Yang, Y. J., and Liu, G. S.: Impact of atmospheric circulations on aerosol distributions in
658 autumn over eastern China: observational evidence, *Atmospheric Chemistry and Physics*, 15, 12115-12138,
659 2015.